

AperTO - Archivio Istituzionale Open Access dell'Università di Torino

Performances of JEM-EUSO: energy and X_{max} reconstruction

This is a pre print version of the following article:

Original Citation:

Availability:

This version is available <http://hdl.handle.net/2318/1578396> since 2016-06-30T15:09:48Z

Published version:

DOI:10.1007/s10686-014-9427-9

Terms of use:

Open Access

Anyone can freely access the full text of works made available as "Open Access". Works made available under a Creative Commons license can be used according to the terms and conditions of said license. Use of all other works requires consent of the right holder (author or publisher) if not exempted from copyright protection by the applicable law.

(Article begins on next page)

1 **Performances of JEM–EUSO: energy and X_{\max}**
2 **reconstruction**

3 **The JEM–EUSO Collaboration**

4
5 Received: date / Accepted: date

6 **Abstract** The Extreme Universe Space Observatory (EUSO) on–board the
7 Japanese Experimental Module (JEM) of the International Space Station aims
8 at the detection of ultra high energy cosmic rays from space. The mission
9 consists of a UV telescope which will detect the fluorescence light emitted
10 by cosmic ray showers in the atmosphere. The mission, currently developed
11 by a large international collaboration, is designed to be launched within this
12 decade. In this article, we present the reconstruction of the energy of the
13 observed events and we also address the X_{\max} reconstruction. After discussing
14 the algorithms developed for the energy and X_{\max} reconstruction, we present
15 several estimates of the energy resolution, as a function of the incident angle,
16 and energy of the event. Similarly, estimates of the X_{\max} resolution for various
17 conditions are presented.

18 **Keywords** JEM–EUSO, Energy Reconstruction, X_{\max} Reconstruction

The JEM–EUSO Collaboration

The full author list and affiliations are given at the end of the paper

Corresponding authors:

F. Fenu (Corr. Author)

¹ Now at: Università degli Studi di Torino, Via Pietro Giuria 1, 10126 Torino, Italy

² Kepler Center for Astro and Particle Physics (IAAT), Sand 1, 72076 Tübingen, Germany

³ Computational Astrophysics Laboratory, RIKEN (ASI), 2–1 Hirosawa, Wako, Japan

⁴ Space and Astroparticle Group (SPAS), Universidad de Alcalá, Alcalá de Henares, Spain

E-mail: francesco.fenu@gmail.com

A. Santangelo (Corr. Author)

Kepler Center for Astro and Particle Physics (IAAT), Sand 1, 72076 Tübingen, Germany

D. Naumov (Corr. Author)

Joint Institute for Nuclear Research, Joliot Curie 6, Dubna, Moscow region, Russia

1 Introduction

The Extreme Universe Space Observatory (EUSO) on-board the Japanese Experimental Module (JEM) of the International Space Station aims at the detection of ultra high energy cosmic particles from space [1]. JEM–EUSO is expected to observe ultra high energy (UHE) cosmic rays above and around the GZK threshold ($E \geq 4 \cdot 10^{19}$ eV), sensibly increasing the exposure with respect to the current generation of ground-based observatories. The expected exposure, virtually unattainable from ground, will most likely open a new observational window on the universe, given the high magnetic rigidity in such an energy range, and will unveil the sources of UHE cosmic rays and the mechanisms of their production. JEM–EUSO is also being designed to explore the neutrino and photon flux at UHE and, therefore, the discrimination capability of the mission for these particles, with respect to charged UHECRs, is critical. Details on the expected science of JEM–EUSO can be found in this issue’s contribution [2] and in the 2013 ICRC contributions [3]. JEM–EUSO mainly consists of a UV telescope sensitive in the 300–400 nm band, which records the fluorescence tracks generated by cosmic rays propagating in the atmosphere with a time resolution of 2.5 microseconds. The detector consists of an array of ~ 5000 Multi Anode Photomultipliers (PMT) organized in 137 PhotoDetector Modules (PDM). Each PMT is then subdivided in 64 pixels of 3×3 mm size, covering a field of view on ground of roughly 500×500 m. The detector therefore consists of more than $3 \cdot 10^5$ pixels, which cover a field of view of 500 km diameter. The structure of the focal surface can be seen in Fig. 1.

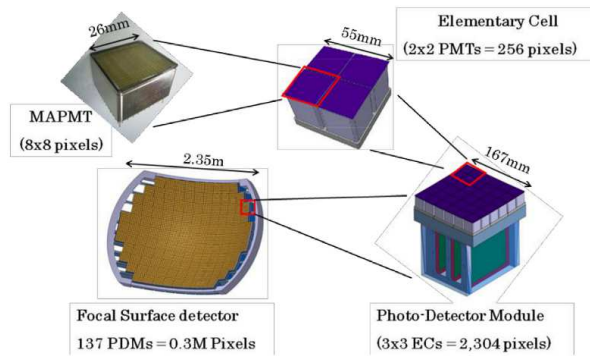


Fig. 1 the JEM–EUSO focal surface structure. From "Report on the phase A study 2010" of the JEM–EUSO collaboration[4].

The instrument will observe the Earth’s atmosphere at night from a height of about 400 km, with a field of view of about 60 degrees. The observed geometrical area will be of $\sim 1.4 \cdot 10^5$ km² and the surveyed atmospheric mass will amount to about $\sim 1.5 \cdot 10^{12}$ tons of air. The instrument payload

is completed by an atmospheric monitoring system, which monitors the cloud coverage and cloud top height of the observed atmospheric scene, as well as, the optical depth of the atmosphere in the region of triggered events. For details of the instrument, we refer the reader to [5], [6], [7]. For each observed event, the arrival time, arrival direction, energy, and X_{\max} must be reconstructed to recover the full observational information.

In this paper, we present the algorithms developed to reconstruct the energy and X_{\max} parameters for events observed by JEM–EUSO. These studies are key to understanding the spectrum and nature of primary particles. The energy resolution also impacts a proper interpretation of the arrival directions map. After a detailed description of the algorithms, we present some preliminary estimates. Such results are only intended as a proof of the established reconstruction chain and are somehow conservative. Since we are continuing with the optimization of the algorithms and with the assessment of the systematics, better values for the JEM–EUSO energy and X_{\max} resolution will be obtained in the future.

The Euso Simulation and Analysis Framework (ESAF) [8] is the simulation software developed in the framework of the ESA–EUSO mission. This software was developed as the mission simulation software to take care of the simulation of all the relevant processes from the shower simulation until the event reconstruction. The ESAF software has been readapted for the new JEM–EUSO instrument and has been used in the present study.

2 Energy and X_{\max} reconstruction

The *PmtToShowerReco* is the energy and X_{\max} reconstruction procedure developed to reconstruct events observed by JEM–EUSO. The reconstruction is structured in several subsequent steps, each of which performing a sub-task. The procedure is used for a first estimate of the shower parameters, like energy and X_{\max} . The method, already described in [9], has been significantly improved and, therefore, a detailed description of the algorithms has been done. A schematic view of this algorithm is given in Fig. 2.

The signal track selection

The *PmtToShowerReco* receives the information in input on the timing and position for all the counts detected on the focal surface. For the analysis we only consider triggered events since this is the condition for data to be sent to ground. More details on the trigger logic can be found in [10]. The PDMs associated with a trigger (and neighboring PDMs) will therefore be sent to ground. In Fig. 3, an example of simulated data received from the instrument can be seen, including both signal and background. This is representing a shower event of $3 \cdot 10^{20}$ eV and 50 degrees zenith angle. At regular intervals, the shower spot crosses the PMTs gaps perpendicularly and, therefore, a decrease in the detected intensity has to be expected. In Fig. 4, the counts detected over the entire shower development time (~ 50 GTUs) are integrated. Here

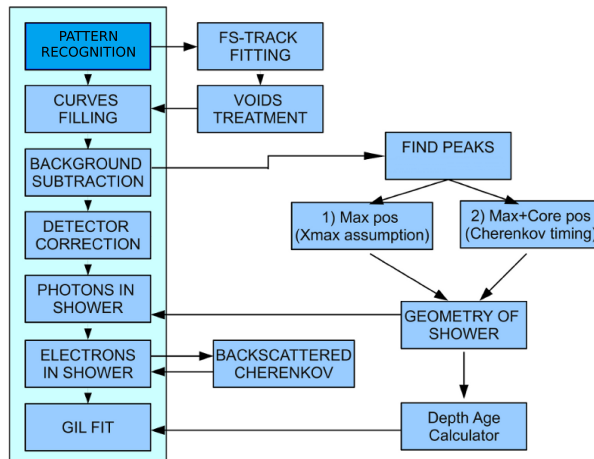


Fig. 2 A simplified view of the *PmtToShowerReco* reconstruction is given here. The input information is represented by the blue box marker with the title *PatternRecognition*. Here information, like the amount of counts for each time and position, is given. Following the vertical path underlined in cyan, the counts curve is transformed according to a series of correction factors which are applied in each step. Complementary operations are executed on the right side of the diagram.

1 we only see the counts that originated from the shower unlike in Fig. 3. The
 2 signal (Fig. 4) cannot be separated from background since the JEM-EUSO
 3 instrument cannot determine whether a photon is originated from a shower or
 4 from airglow. Nevertheless, a clear concentration of signal is visible already on
 5 the raw data of Fig. 3. In fact, the shower signal can be imagined as a spot
 6 moving on the focal surface with a speed equal to the projection of the shower
 7 speed. In Fig. 5, the temporal evolution of the track can be observed. The
 8 shower signal has been represented in colors depending on the photons arrival
 9 time. Five temporal windows, each of 10 GTUs ($25 \mu\text{s}$), have been identified.
 10 This particular shower is, therefore, clearly evolving to the right of the image
 11 for a time duration of roughly 50 GTUs.

12 The first task of the reconstruction must be the identification of the pixels
 13 and GTUs with signal. Several algorithms have been developed for this pur-
 14 pose. In this work, two have been used, namely the *LTPPatternRecognition*
 15 and the *PWISE* algorithms [11] [9]. A detailed discussion of the two algorithms
 16 is out of the scope of this publication but both of them are looking for signal
 17 excesses concentrated in space and moving in a coherent way. As can be seen
 18 in Fig. 6 and 7, both such selections follow the real track shown in Fig. 4.
 19 On the basis of what was identified by the pattern recognition for each GTU,
 20 we calculate the center of mass of the spot. All the pixels whose center falls
 21 within a 3.5 mm radius are chosen for the construction of the signal curve. This
 22 choice has been made in order to select an area that is on average equal to the

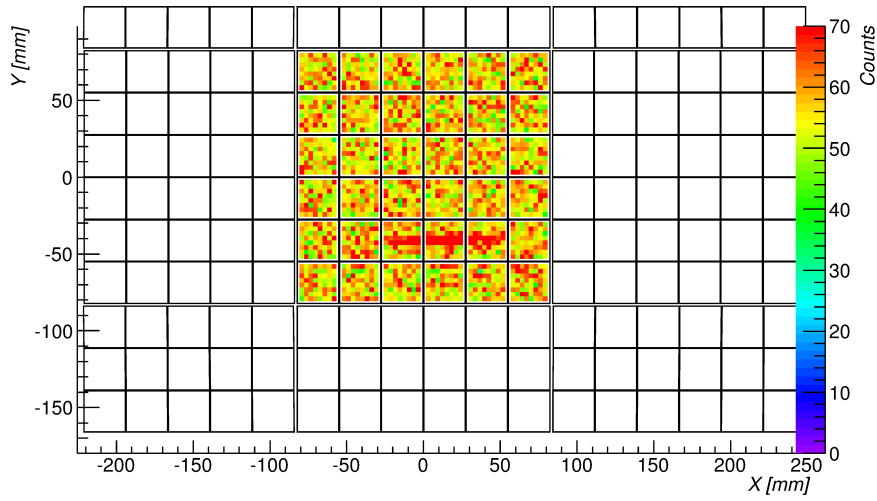


Fig. 3 the data received from the instrument. As can be seen here, background and signal photons cannot be distinguished. The color scale represents the integrated number of counts.

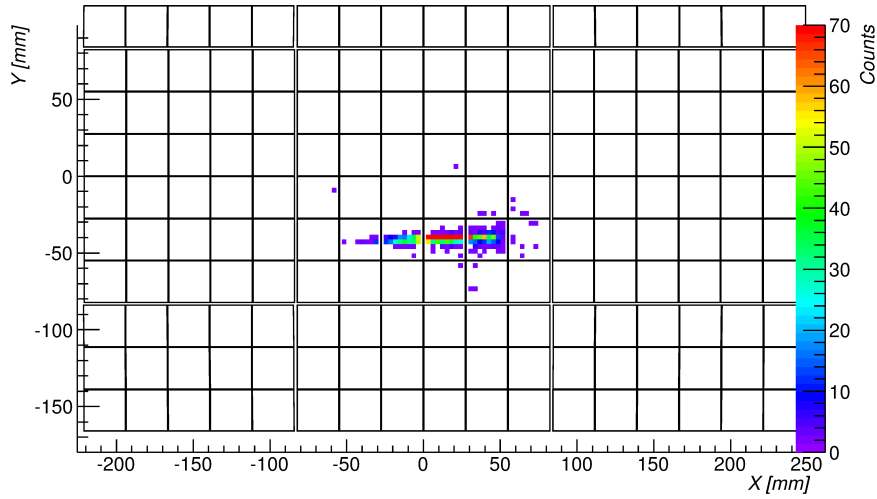


Fig. 4 the simulated track is shown here. We only see the counts originated by the shower. The color scale represents the integrated number of counts.

- 1 collection area of the *OpticsResponse* (See paragraph *The detector correction*
- 2 for more explanations).

3 **The signal curve reconstruction**

- 4 The first step of the *PmtToShowerReco* consists of the reconstruction of the so-
- 5 called curve of counts, in other terms, the number of counts per GTU detected
- 6 by the instrument. The information of the reconstructed track (based on Figs.

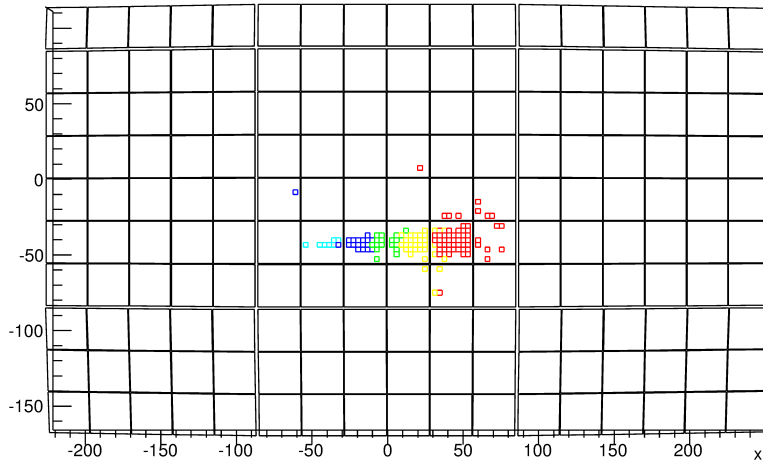


Fig. 5 the evolution in time of the shower simulated track. The color scale represents 5 different time windows in which simulated photons reach the detector.

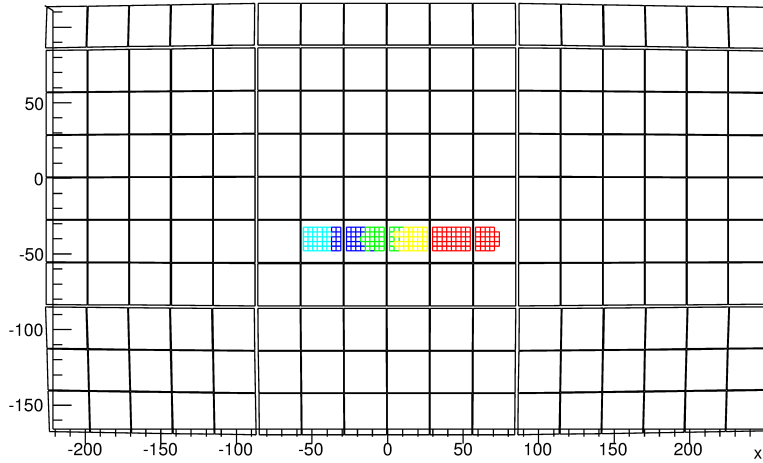


Fig. 6 the signal selection according to the *LTPPatternRecognition* algorithm. In color scale, 5 time windows each of 10 GTUs can be seen.

1 6 or 7) is read out and the timing for all the counts in the selected data is
 2 used to obtain the signal intensity as function of time.

3 In parallel, we calculate the average position for each time frame in order
 4 to assess possible signal losses due to focal surface voids. In fact, when the
 5 spot approaches the gaps between PMTs a part of it will fall onto a non
 6 sensible area of the detector. A decrease of the signal intensity then must
 7 be expected. Such loss will cause systematics in the energy reconstruction.

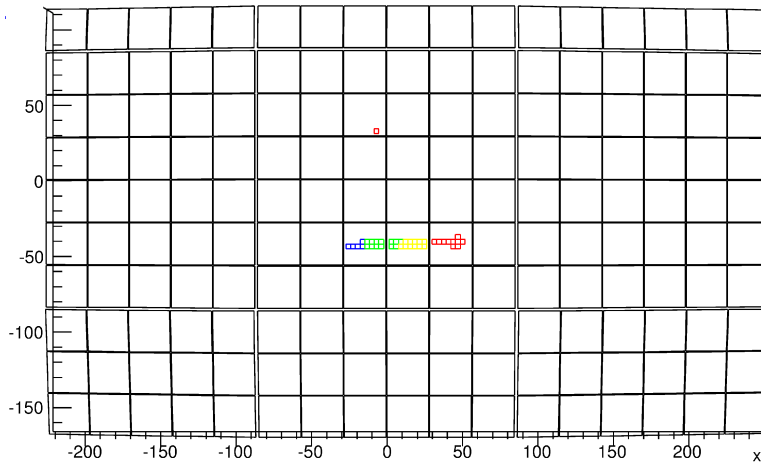


Fig. 7 the signal selection according to the *PWISE* algorithm. In color scale, 5 time windows each of 10 GTUs can be seen.

1 Two possibilities are open for removing this problem. When the signal for a
 2 particular time frame is close to focal surface gaps, it must be either removed
 3 or corrected. In the present study, all the points falling within 3 mm from the
 4 gaps are removed since no sufficiently detailed spot parameterization has yet
 5 been developed. Such a radius is chosen, taking into account the projection of
 6 the shower lateral distribution, so that it will include most of the JEM–EUSO
 7 signal.

8 An essential step of the reconstruction chain is the correction of the back-
 9 ground. Depending on the selected area, in fact, the background component
 10 must be subtracted from the signal intensity curve. In fact, the identification
 11 of the pixel–GTU with signal does not mean the identification of pure sig-
 12 nal. Such pixel GTUs will still be contaminated by a certain amount of pho-
 13 tons from airglow background. The knowledge of such a contamination can
 14 be achieved very easily by long time measurements of the diffuse Earth emis-
 15 sion. The knowledge of the average background therefore allows the correction
 16 of a certain amount of counts each GTU. A constant background amount is
 17 subtracted for each selected pixel–GTU.

18 The counts curve is therefore built, according to the previously described
 19 selection, and the background is subtracted. An example of such a curve for
 20 the analyzed event can be seen in Fig. 8. In this figure, the reconstructed curve
 21 (points with error bars) is superposed with the simulated curve (continuous
 22 curve). As can be seen, the two curves are in good agreement except for the
 23 regions where gaps are present (gray areas).

24 **The peak identification**

25 The identification of the maximum and Cherenkov peak of the reconstructed
 26 light curve is also critical. The search for these features is not trivial.

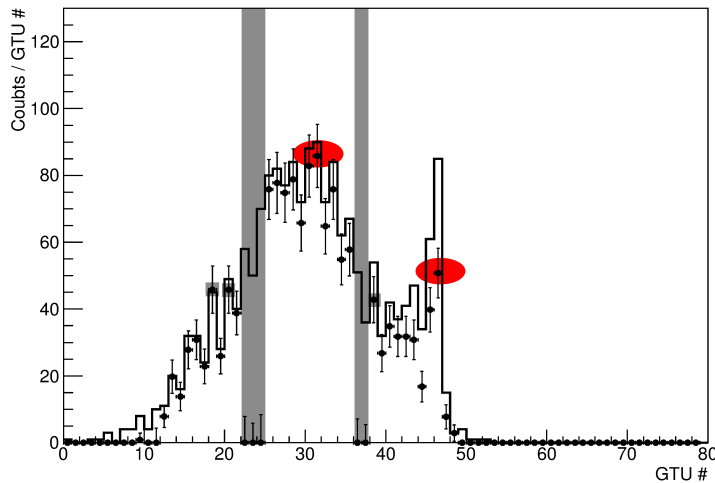


Fig. 8 The simulated (line) and reconstructed (points) detector counts curve. Highlighted with squares, are the bins recognized as peaks by the procedure. Highlighted with ellipses, are the peaks identified as Cherenkov and maximum. Two gaps can be observed as shaded areas. The current configuration sets the signal in the vicinity of a gap to zero. The simulated event has an energy of $3 \cdot 10^{20}$ eV and a zenith angle of 50 degrees.

1 Depending on the zenith angle and on the nature of the diffusing surface¹,
 2 the Cherenkov reflected component can be rather spread, implying a reduction
 3 of the signal to noise ratio. For these reasons, the automatic recognition of a
 4 physically reasonable peak is not trivial, and not always possible, and requires
 5 a dedicated analysis. The algorithm takes into account the most common cases
 6 and tries to cope with them in order to recognize the highest fraction of events
 7 showing the Cherenkov mark.

8 A cleaning of the signal is necessary to avoid the detection of fake peaks,
 9 in particular, toward the later stages of the event, where the signal is low. In
 10 fact, especially for high zenith angles, events can be characterized by long tails
 11 due to the backscattering of the photons in atmosphere. For this purpose, a
 12 search in a ± 2 window around each bin is done. If the bin is isolated, namely
 13 if more than 3 bins out of 5 are equal to zero, it will not be considered for
 14 the peak search. The isolated bin will still be considered if its intensity is over
 15 a certain threshold (10 counts), since it is unlikely that backscattering can
 16 generate such a strong, timely constrained bin.

17 As a next step, all peaks in the counts curve are identified. The peak is
 18 defined assuming that a bin is the maximum between the ± 2 adjacent bins.
 19 In other words, if the bin is larger than (or equal to) the ± 2 bins around it,
 20 it will be considered as a peak. Another requirement for a bin to be accepted as
 21 a peak is its amplitude. If the peak is at least of amplitude 10 counts, it will

¹ The Cherenkov reflection will be modelled as a Lambertian reflector with an albedo of 5%.

1 be accepted otherwise, it will be rejected. This is done in order to reduce fake
 2 peaks due to background fluctuations. We then analyze the detected peaks to
 3 find the temporal position of the Cherenkov mark and the maximum. After the
 4 cleaning described above, the last peak can usually be identified as a prelim-
 5 inary Cherenkov peak. However, cuts must be applied on the peak to reduce
 6 the probability of fake Cherenkov identification. For example, the duration of
 7 the shower after the preliminary Cherenkov is a valid selection parameter. In
 8 fact, the Cherenkov reflection peak should, in most cases, represent the end of
 9 the shower. The presence of significant amounts of light after the peak is most
 10 likely an indication of a fake Cherenkov reconstruction. This is happening in
 11 most of the showers with a zenith angle above 60 degrees. Any peak after the
 12 maximum could, in fact, be identified as preliminary Cherenkov. A further se-
 13 lection criterion can be applied on the time separation between the Cherenkov
 14 and maximum. The knowledge of the reconstructed shower zenith angle [12]
 15 and the assumption of a shower parameterization will set constraints on the
 16 minimum time separation between maximum and Cherenkov. In fact, direc-
 17 tion and a shower parameterization will turn into an estimate of the maximum
 18 altitude. Such an altitude will, therefore, translate into a minimum time sep-
 19 aration between maximum and the impact on ground. Further criteria on the
 20 peak intensity can be chosen in order to minimize the risk of fake detection.

21 The maximum will usually be usually as the peak with the maximum
 22 intensity, excluding the preliminary Cherenkov. In the case that more maxima
 23 have the same amplitude, the average between the peaks GTU number is
 24 considered. Moreover, maxima near gaps are considered in a devoted way. In
 25 fact, if the most intense peak is in the vicinity of a gap it will most likely be
 26 affected by systematics. If strong secondary peaks are present (with at least
 27 90% the intensity of the maximum), the weighted average between their timing
 28 and the maximum will be calculated. This will be considered to be the the best
 29 estimation of the maximum.

30 An example of peak search is given in Fig. 8 where the peaks are analyzed.
 31 As can be seen, the Cherenkov and maximum peaks have been correctly iden-
 32 tified and highlighted with red ellipses. Minor peaks have also been found and
 33 underlined with gray squares². As can be seen, their vicinity to gaps makes
 34 it clear that peaks are more likely to occur in this situation. This, however,
 35 does not hamper the search for the maximum or for the Cherenkov peak. A
 36 preselection, excluding peaks near gaps, has not been performed to avoid loss
 37 of maxima or Cherenkov falling near the PMT boundary. Optimization work
 38 can be still done to reduce the number of gap-related peaks.

In Fig. 9, the evaluation of the quality of the peak search is given for 100
 events of 10^{20} eV, 50 degrees. Here, we plot the reconstruction quality of the
 maximum and Cherenkov according to Eq. 1 and 2

$$\Delta_{cher} = GTU_{cher}^{reco} - GTU_{cher}^{simu} \quad (1)$$

² A small note should be given on the peaks on GTUs 18 and 20. These peaks are identified given the very unlikely case of peaks of exactly the same amplitude within ± 2 GTUs. The condition chosen for a bin to be accepted as peak is \geq .

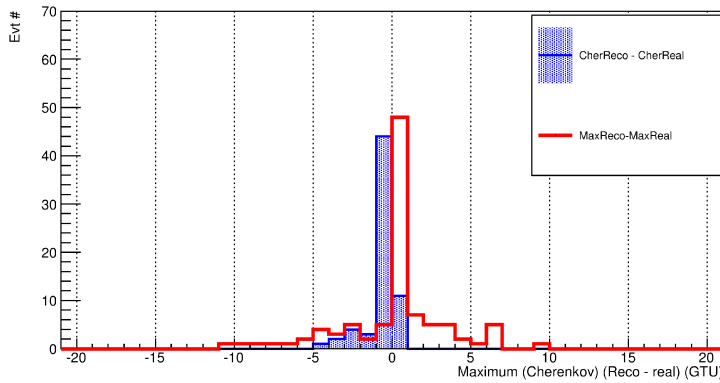


Fig. 9 The quality of the maximum and Cherenkov peaks reconstruction. Plotted here is the difference between reconstructed and simulated maxima and Cherenkov for 100 events.

$$\Delta_{max} = GTU_{max}^{reco} - GTU_{max}^{simu} \quad (2)$$

1 The maximum distribution is centered on 0.2 and has an RMS of 3 GTUs.
 2 The Cherenkov peak is centered on -0.65 and has an RMS of 1 GTU. This
 3 shows how the maximum is more sensible on fluctuation and on the presence of
 4 gaps than the Cherenkov. Moreover, 65 events out of 100 have been recognized
 5 with Cherenkov while the maximum has been recognized in all 100 events.

6 The detector correction

7 The photons curve on the focal surface is then reconstructed. To reach this
 8 step, we use a parameterization of the photo-detector, which includes the
 9 efficiency of the PMTs, the loss of the front end and the transmittance of the
 10 optical filter.

11 Following that, we correct the effects of the optics, taking into account the
 12 optics efficiency, using the *OpticsResponse* of ESAF. This map is produced
 13 with aid of a script run outside of the main reconstruction frame. In order to
 14 calculate the *OpticsResponse* map, several point sources are simulated follow-
 15 ing a set of predefined incident angles and wavelengths. The optics efficiency
 16 factor is calculated for each direction as in Eq. 3.

$$\varepsilon_{opt} = \frac{\gamma_{encirc}}{\gamma_{opt}} \quad (3)$$

17 The so-called trigger throughput ε_{opt} is affected both by the performances
 18 of the optics and by the physical width of the shower [13], and is the ratio of the
 19 photons reaching the focal surface within a predefined collection area γ_{encirc} ,
 20 with respect to the photons incident on the pupil γ_{opt} . The photons landing
 21 outside of the collection area have been considered not detectable since they
 22 are indistinguishable from the background. A collection area of 3 mm radius
 23 has been chosen in the present work. This choice is justified considering that

1 most of the signal falls in a circular area of 3 mm radius. The center of this
 2 area is chosen as the point with the maximal photon density.

3 Other essential information is the mapping of the arrival directions as a
 4 function of the pixel identification number, namely the so-called *PixelAn-*
 5 *gleMap*. The *PixelAngleMap* allows the reconstruction of the arrival direction
 6 of the photons seen by any pixel. This map is also produced with the aid of
 7 a script run outside of the main reconstruction frame. The script produces
 8 a large amount of photons of various wavelengths diffusively shining on the
 9 pupil. The off-axis angle is chosen to vary continuously from 0 to well above
 10 the JEM–EUSO field of view (± 45 degrees) to consider the effect of stray
 11 light. The wavelength is ranging from 250 to 500 nm. The distribution of ar-
 12 rival direction for all the photons landing on each pixel will be produced and
 13 its average will be saved in the *PixelAngleMap*.

14 The maps described above allow the calculation of an efficiency factor
 15 for each phase of the event development. This efficiency factor is needed to
 16 calculate the photon curve at the optics entrance. The final output of the chain
 17 is in fact an estimated *photon curve* at the entrance pupil. The simulated and
 18 the reconstructed photons curve on pupil can be seen in Fig. 10 for the same
 19 event shown above.

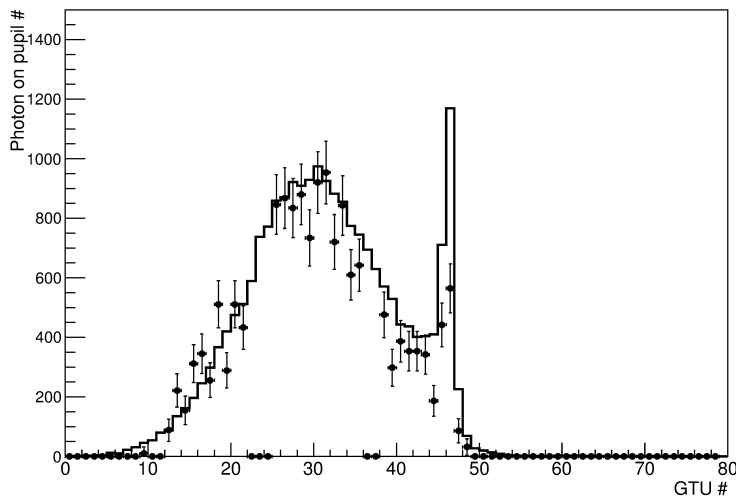


Fig. 10 the simulated (line) and reconstructed (points) pupil photon curve. The simulated event has an energy of $3 \cdot 10^{20}$ eV and a zenith angle of 50 degrees.

20 The shower's luminosity reconstruction

21 At this stage, the luminosity of the shower must be calculated. For this pur-
 22 pose, we need to know the shower position as a function of time. This is
 23 necessary in order to estimate the distance of the shower from the detector

1 and consequently, the total amount of photons produced. Given the total num-
 2 ber of photons at the pupil and the $\frac{1}{d^2}$ flux decrease factor, it is possible to
 3 reconstruct the number of photons at the shower site. The knowledge of the
 4 shower position in the earth's atmosphere is also needed to properly apply all
 5 corrections relative to the atmospheric absorption and scattering.

6 To reconstruct the position of the shower in the atmosphere, we use two
 7 alternative procedures. The first makes use of the Cherenkov reflection mark,
 8 while the second assumes a parameterization for the depth of the maximum
 9 (X_{\max}) and relies on the direction estimated with the angular reconstruction
 10 procedure [12].

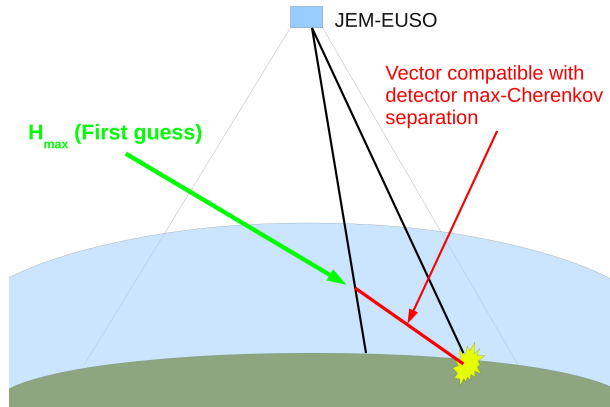


Fig. 11 the Cherenkov H_{\max} reconstruction method. This algorithm requires the reconstruction of both maximum and Cherenkov peak. The separation time between the two events at the detector and the altitude of the ground gives information on the altitude of the maximum.

11 The first method shown in Fig. 11 assumes the identification of a Cherenkov
 12 mark in the light curve. The time delay between the shower maximum and the
 13 Cherenkov mark allows the distance traveled by the shower to be calculated.
 14 This is easily understood from basic kinematics, considering that showers prop-
 15 agate at the speed of light. Knowing the projection of the maximum and of the
 16 Cherenkov mark, it is possible to infer the altitude of the maximum itself. In
 17 fact, the detection of the Cherenkov mark, in clear sky conditions, constrains
 18 the position of the shower at the ground level within a very narrow time win-
 19 dow. In other terms, the timing and position of both peaks will efficiently
 20 constrain the zenith angle of the shower.

21 The second method is schematically shown in Fig. 12. and relies on the
 22 prior reconstruction of the direction [12] and on the knowledge of the maximum
 23 projection onto the field of view. An H_{\max} is determined according to the depth
 24 of the points in the projected maximum along the shower direction (see Fig 12).

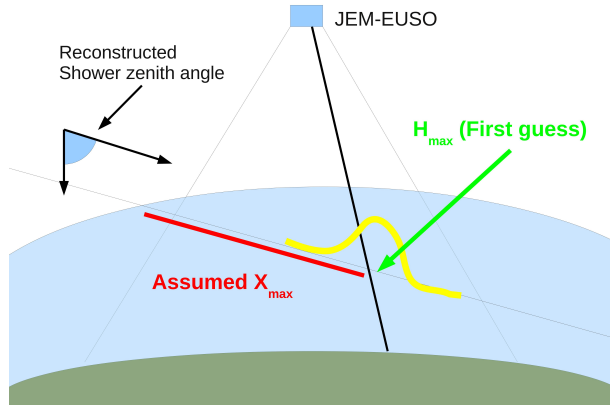


Fig. 12 the slant depth H_{\max} reconstruction method. This algorithm requires the reconstruction of the shower direction and an assumption on the slant depth of the maximum. This set of parameters constrains the altitude of the maximum in atmosphere.

1 Of course, X_{\max} depends on the nature of the primary. Therefore, a distinction
 2 must be made between the assumed X_{\max}^{geo} and the resulting X_{\max}^{fit} obtained
 3 from the fit. We stress that the entire procedure must be iterated to obtain the
 4 best possible geometry reconstruction and get rid of the initial assumptions on
 5 X_{\max}^{geo} .³ The results obtained through this method will be biased by the initial
 6 assumption on X_{\max}^{geo} . However, the energy sensibility to the bias is contained
 7 within 10%, as long as, the altitude is reconstructed within 2 km accuracy.
 8 The X_{\max}^{fit} must be treated more carefully, since a few hundred meters altitude
 9 bias can already result in a strong bias on the slant depth of the maximum.

10 The knowledge of the maximum position and shower direction allows the
 11 calculation of the shower position and slant depth for all times. The atmo-
 12 spheric profile (US Standard 1976 Atmosphere [14]) is used together with the
 13 reconstructed shower's direction and position to integrate the atmospheric
 14 density until the top of the atmosphere. We also estimate the shower age from
 15 the information on the position of the maximum.

16 Knowing the position and the shower's age as a function of time, we can
 17 estimate the energy distribution of the secondary electrons. We use, for this
 18 study, the parameterization from [15].

19 The knowledge of the produced spectrum is then used for the estimate
 20 of the scattering and absorption in atmosphere. At this stage, the shower
 21 luminosity estimation is concluded. In fact, by knowing the position of the

³ A complete explanation on the iteration procedure is out of the scope of this publication. The iteration will be performed by varying the shower parameters obtained through the first reconstruction run. The reconstruction will be applied backward and the detector response obtained in this way will be compared with what originally detected by JEM-EUSO. The deviation of this test from the data will define a confidence interval in the parameter space and possibly deliver a better set of parameters than what was found in the first run.

1 shower inside the atmosphere and the produced spectrum, the modelization of
 2 the transmittance can be performed. For this purpose, the standard *lowtran*
 3 software has been chosen [16]. In Fig. 13, the reconstructed and simulated
 4 shower luminosity can be seen for the usual $3 \cdot 10^{20}$ eV 50 degrees event.

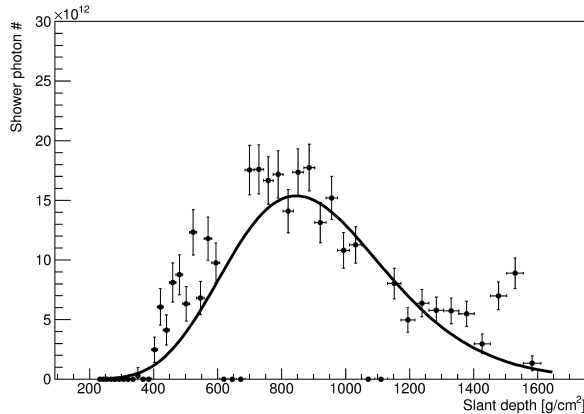


Fig. 13 The simulated (line) and reconstructed (points) shower photon curve (shower luminosity). The simulated event has an energy of $3 \cdot 10^{20}$ eV and a zenith angle of 50 degrees.

5 The shower profile reconstruction and fit

6 After calculating the luminosity as function of location and slant depth, the
 7 shower profile is reconstructed. The knowledge of the fluorescence [17] and
 8 Cherenkov ⁴ yield then allows for the reconstruction of the electrons curve
 9 of the shower. Unfortunately, no distinction is possible on whether the recon-
 10 structed photons are originating from fluorescence or backscattered Cherenkov
 11 light (See Fig. 14 for an explanation of the signal composition). An iterative
 12 procedure is being developed in order to disentangle the two components . An-
 13 other possibility is the one described in [18]. However, the present results are
 14 not including such corrections and the final result will be affected by an over-
 15 estimation of the energy due to such contamination. The systematics brought
 16 by the missing correction of the Cherenkov contamination⁵ have been assessed
 17 and will be corrected later.

18 The obtained electron curve is fitted to obtain the energy and X_{\max} param-
 19 eters. In the present study, we have chosen the GIL function [19][20][21][22]
 20 for the fit, but any other function can be applied. The fit parameters of the
 21 function are simply the energy and the X_{\max} . A fluctuation in the width of the

⁴ According to the standard theory the Cherenkov yield is equal to $C_Y(E, h) = 2\pi\alpha \left(2\delta - \left(\frac{m_e c^2}{E}\right)^2\right) \left(\frac{1}{\lambda_{\min}} - \frac{1}{\lambda_{\max}}\right)$ where α is the fine structure constant, δ is $n-1$ (n is the refractive index), E the electron's energy, λ_{\min} and λ_{\max} are the integration extremes.

⁵ The backscattered component is therefore not distinguishable from fluorescence and has to be corrected.

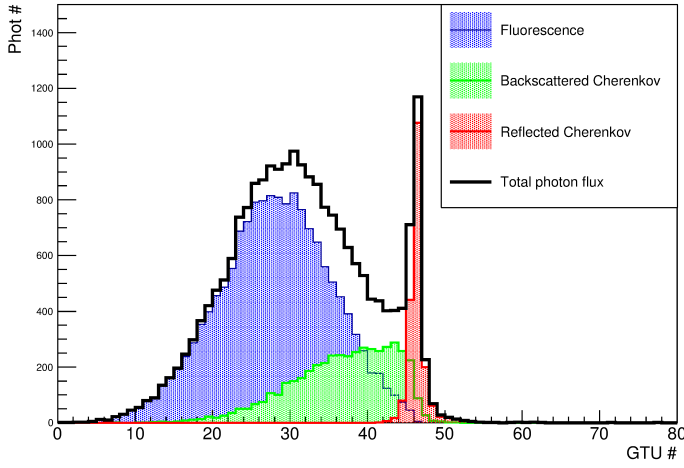


Fig. 14 the curve of photons at the pupil. In different colors, we show the different components of the light curve. In blue, we can see the direct fluorescence, in green, we can see the backscattered Cherenkov and, in red, we see the reflected Cherenkov. As black line, we see the total signal. The simulated event has an energy of $3 \cdot 10^{20}$ eV and a zenith angle of 50 degrees.

- 1 profile is not included in the parameterization. The guide event shown above
- 2 is also represented in Fig. 15, where real and reconstructed profiles are plotted together with the fit on the reconstructed points.

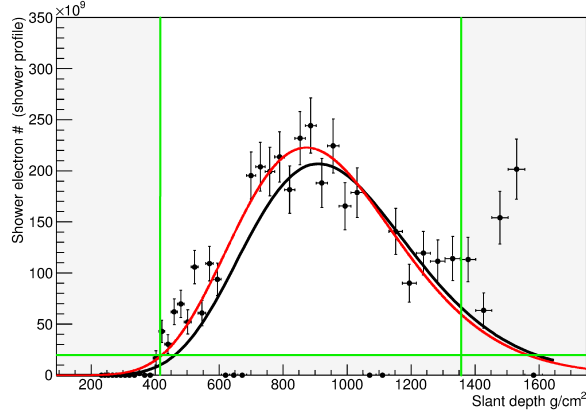


Fig. 15 the simulated (black line) and reconstructed (points) shower electron curve. As a red line, the GIL fit can be observed. The simulated event has an energy of $3 \cdot 10^{20}$ eV and a zenith angle of 50 degrees. The reconstructed parameters for this fit are $3.22 \cdot 10^{20}$ eV and 873 g/cm^2 (whereas the real X_{\max} was 915 g/cm^2). The χ^2 per event is 0.905. The shaded areas show the points which are excluded from the fit.

We run the fit algorithm only on the points which are above a certain threshold in order to avoid the contamination of the result with the background dominated points. Furthermore, we select those points inside a window around maximum. This is done to exclude the Cherenkov peak.

The procedure described above and summarized in the diagram of Fig. 2 can be summarized with the following equation 4.

$$\begin{aligned} \frac{dN_{pe}}{dL} = & \int_{\lambda_{\min}}^{\lambda_{\max}} \left\{ N_e \left(X(L), A, E \right) \epsilon_{\text{FY}}^\lambda \left(H(L), s(L) \right) \frac{1}{4\pi} \right. \\ & + \Psi_{\text{CH}}(\lambda, \vec{P}(L)) \left. \right\} \frac{A_{\text{opt}} \cos \theta}{R^2} T_s \left(\lambda, \vec{P}(L), \vec{D} \right) \\ & \cdot T_a \left(\lambda, \vec{P}(L), \vec{D} \right) \epsilon_{\text{opt}} \left(\lambda, \theta, \phi \right) T_{\text{BG3}} \left(\lambda \right) \epsilon_{\text{PMT}} \left(\lambda \right) \epsilon_{\text{FE}} d\lambda \end{aligned} \quad (4)$$

The equation shows the amount of counts detected by JEM-EUSO for every element dL of the shower development. This number depends on the number of electrons in the shower $N_e \left(X(L), A, E \right)$, parameterized as function of the energy E , on the atomic mass A and of the single step slant depth. $\epsilon_{\text{FY}}^\lambda \left(H(L), s(L) \right)$ is the fluorescence yield (in differential notation for each wavelength) which depends both on altitude and on the age of the shower. The dimension of the entrance pupil is expressed by the area A_{opt} which also includes a $\cos(\theta)$ factor to take into account the photons arrival direction. The efficiency of the detector is given by $\epsilon_{\text{opt}} \left(\lambda, \theta, \phi \right)$, $\epsilon_{\text{PMT}} \left(\lambda \right)$, ϵ_{FE} and $T_{\text{BG3}} \left(\lambda \right)$ which respectively represent the throughput efficiency of the optics, the detector efficiency of the PMT, the losses of of the front end electronics and the transmittance of the optical adaptor. Finally, the Rayleigh and ozone absorption are considered in $T_s \left(\lambda, \vec{P}(L), \vec{D} \right)$ and $T_a \left(\lambda, \vec{P}(L), \vec{D} \right)$, which depend on wavelength, shower and detector position. The function must be integrated from the minimum to the maximum wavelength and depends on the position which the shower occupies for each dL .

A specific treatment is needed to estimate the Cherenkov contamination $\Psi_{\text{CH}}(\lambda, \vec{P}(L))$. In Eq. 5, the additional component (in counts) due to Cherenkov and for each shower step is given:

$$\begin{aligned} \Psi_{\text{CH}}(\lambda, \vec{P}(L)) = & \int_0^L \left[N_e \left(X(l), A, E \right) \epsilon_{\text{CH}}^\lambda \left(H(l), s(l) \right) \right. \\ & \cdot T_s \left(\lambda, \vec{P}(l), \vec{P}(L) \right) T_a \left(\lambda, \vec{P}(l), \vec{P}(L) \right) \left. \right] dl \\ & \cdot \left(-\dot{T}_s \left(\lambda, \vec{P}(L) \right) dl \right) \alpha_{\text{anys}} \end{aligned} \quad (5)$$

1 What can be seen here is the integral from 0 to the actual shower longitudinal
 2 development of the whole propagating Cherenkov photon population. The
 3 number of electrons for each of the past steps of a shower $N_e \left(X(l), A, E \right)$ has
 4 to be considered together with the Cherenkov yield $\epsilon_{\text{CH}}^\lambda \left(H(l), s(l) \right)$ integrated
 5 over the secondary energy spectrum. For each of the dl elements, the produced
 6 photons must be carried to the L point. The propagation is affected by losses
 7 $T_s \left(\lambda, \vec{P}(l), \vec{P}(L) \right) T_a \left(\lambda, \vec{P}(l), \vec{P}(L) \right)$ respectively for scattering and ozone
 8 absorption. The derivative on dl of the the scattered fraction $\left(-\dot{T}_s \left(\lambda, \vec{P}(L) \right) \right)$
 9 calculated at the L position multiplied by the differential dl describes how
 10 much of the transmitted light is scattered in the interval dl . It is well known
 11 that the Rayleigh scattering is not isotropic and, therefore, a component α_{anys}
 12 must account for the asymmetry of the scattered photons.

13 The systematics estimation

14 The biases on the reconstructed parameters have also been analyzed in detail.
 15 Samples of events have been simulated in fixed conditions and reconstructed.
 16 Each of the previously described reconstruction steps has been therefore compared
 17 with the corresponding step in the simulation framework. In other terms,
 18 we perform a comparison between the model of the reconstruction and the
 19 Montecarlo. This is done to test the quality of the modeling with respect to
 20 the simulation.

21 We can, for example, take any of the Fig. 8, 10, 13 or 15 and calculate
 22 the correction factor applied in any of the reconstruction steps and compare
 23 it with the simulation. In the first case, for example, we would be calculating
 24 for each GTU the ratio between the reconstructed curves of Figs. 13 and 15
 25 (the points) . Following that, we compare this ratio with the ratio between
 26 the continuous lines which represent the simulated curves. This expresses the
 27 deviation of a particular reconstruction step from the simulation. A schematic
 28 visualization of this process can be seen in Fig. 16.

29 Let us consider the simulation branch of Fig. 16. Being $N_{\text{sim}}^n(t, \text{evt})$ and
 30 $N_{\text{sim}}^{n-1}(t, \text{evt})$ the number of counts at the steps n and $n - 1$ for a time t and
 31 event evt , we define $\epsilon_{\text{sim}}(t, \text{evt})$ as the "efficiency" factor for an event evt , at
 32 the time t and between the simulation steps n and $n - 1$.

$$\epsilon_{\text{sim}}(t, \text{evt}) = \frac{N_{\text{sim}}^n(t, \text{evt})}{N_{\text{sim}}^{n-1}(t, \text{evt})} \quad (6)$$

33 In the same way for the reconstruction branch, we define $N_{\text{reco}}^m(t, \text{evt})$ and
 34 $N_{\text{reco}}^{m+1}(t, \text{evt})$ which represent the number of counts at the steps m and m
 35 + 1, for event evt and time t . This brings us to the definition of the factor
 36 $\epsilon_{\text{reco}}(t, \text{evt})$ representing the correction factor applied between the m^{th} and
 37 $m^{\text{th}} + 1$ reconstruction steps instead.

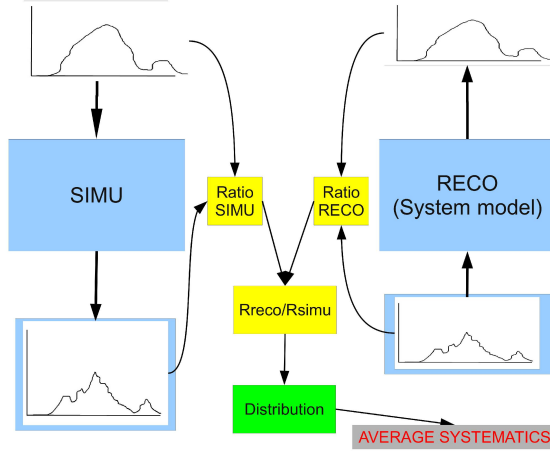


Fig. 16 the logic of the systematic estimation algorithm. A generic step is depicted. The ratio between input and output will be calculated for both reconstruction and simulation. The discrepancy of each reconstruction step from the simulated will be estimated for each event. The median on the distribution of the deviations will be defined as systematics (see gray box).

$$\epsilon_{\text{reco}}(t, \text{evt}) = \frac{N_{\text{reco}}^m(t, \text{evt})}{N_{\text{reco}}^{m+1}(t, \text{evt})} \quad (7)$$

1 Both n and m are indexes chosen to identify the simulation–reconstruction
 2 step and they are chosen from 0 to $N_{\text{max}} = M_{\text{max}}$. The index is defined in order
 3 to follow the "flux" of the operations. For this reason, n goes from shower to
 4 detector while m from detector to shower. Therefore, n must be defined to be
 5 equal to $N_{\text{max}} - m$ (or $M_{\text{max}} - m$) in order to guarantee the correspondence
 6 between simulation and reconstruction steps. The ratio between the two factors
 7 is then mediated over all the event GTUs

$$\Delta^k(\text{evt}) = \frac{\sum_{t=0}^{t_{\text{max}}} \frac{\epsilon_{\text{reco}}(t, \text{evt})}{\epsilon_{\text{sim}}(t, \text{evt})}}{t_{\text{max}}} \quad (8)$$

8 giving the average bias of the single event for a specific condition k (for
 9 example angle, energy, primary type, position...). For a fixed condition k , a
 10 sample of events has been simulated and the $\Delta^k(\text{evt})$ factor calculated. The
 11 median of the distribution of the $\Delta^k(\text{evt})$ factor has been assumed to be the
 12 bias of the reconstruction on a particular step for a condition k . This esti-
 13 mation has been performed in different conditions and for all the correction
 14 steps applied in the reconstruction. This is the case for the focal surface (Fo-
 15 calSurf), optics (Opt), atmospheric transmission (Transmitt) and fluorescence
 16 yield (FluorYield) of Tab. 1.

1 The factor (CTSSel), on the other hand, represents the collection ineffi-
 2 ciency. This is simply calculated as the mediated ratio between reconstructed
 3 and simulated counts curve.

$$\Delta_{CTS}^k(\text{evt}) = \sum_{t=0}^{t_{\max}} \frac{CTS_{\text{reco}}(t, \text{evt})}{CTS_{\text{sim}}(t, \text{evt})} \quad (9)$$

4 The factor $CTS_{\text{reco}}(t, \text{evt})$ represents the reconstructed counts curve while
 5 the $CTS_{\text{sim}}(t, \text{evt})$ represents the simulated. This ratio is then mediated
 6 over all the GTUs. The median over all the $\Delta_{CTS}^k(\text{evt})$ will finally be put in table
 7 1 (under CTSSel) to represent how much of the simulated shower signal can
 8 be collected by the reconstruction algorithms in the condition k .

The contribution of the backscattered Cherenkov and the systematics of
 the geometrical uncertainties have been also estimated. In fact, in the stan-
 dard configuration for the systematics study, the Cherenkov backscattering
 has been deactivated. In the same way, the reconstruction of the geometry
 is not considered and the reconstruction is performed with the simulated ge-
 ometry. In this way, we try to disentangle different sources of systematics.
 We, therefore, simulate a sample of events in the same condition as in the
 standard case, but with the backscattered Cherenkov. The same is done for
 the geometrical reconstruction, where the sample is reconstructed using the
 reconstructed geometry. The ratio between the reconstructed energy obtained
 in standard condition and the new values are assumed to be the systematic
 brought by the non correction of the backscattered Cherenkov or by the geom-
 etry reconstruction. In Eq. 10, the reconstructed energy $E_{\text{reco}}^*(\text{evt})$ is obtained
 by using either the reconstructed geometry or by including the backscattered
 Cherenkov, while the $E_{\text{reco}}^{**}(\text{evt})$ is the standard case with no backscattered
 Cherenkov and reconstruction performed with real geometry.

$$\Delta_{\text{geo./backscatt.}}^k(\text{evt}) = \frac{E_{\text{reco}}^*(\text{evt})}{E_{\text{reco}}^{**}(\text{evt})} \quad (10)$$

9 The median over the factors for all the events evt will be calculated and
 10 again reported in Tab. 1 (CherBack and GeoReco).

11 The Total factor is calculated as shown in Eq. 11 and represents the total
 12 systematic effects which have been identified.

$$\text{Total} = \text{CTSSel} \times \text{FocalSurf}^{-1} \times \text{Opt}^{-1} \times \text{Transmitt}^{-1} \times \text{FluorYield}^{-1} \times \text{CherBack} \times \text{GeoReco} \quad (11)$$

13 This factor is the product of all the biases but has some of them in the
 14 denominator. This is due to the fact that such factors represent the mismatch
 15 between the correction factor, with respect to the Montecarlo. The correction
 16 is always applied at the denominator and, therefore, an overestimation of the
 17 correction leads to an underestimation of the reconstructed energy.

18 More details can be found in [23] but one example is shown in Tab. 1 where
 19 several samples of 8000 events impacting near the center with different zenith

Zenith (deg)	CTSsel	FocalSurf	Opt	Transmitt	FluorYield	CherBack	GeoReco	Total
30	0.97	1.03	0.95	0.98	0.99	1.23	1.06	1.33
45	0.94	1.02	0.95	0.99	0.99	1.16	1.06	1.21
60	0.92	0.99	0.96	1	0.99	1.09	1.06	1.13
75	0.87	1	0.95	1.01	0.99	1.02	1.03	0.96

Table 1 an example of the reconstruction bias is shown here. The chosen energy is 10^{20} eV, the events are impacting in the square ($\pm 20, \pm 20$) km and the ϕ angle has been chosen from 0 to 360 degrees. The event zenith angle (θ), the bias on the signal selection (CTSsel), on the detector efficiency correction (FocalSurf), on the optics (Opt), on the transmittance (Transmitt), on the fluorescence yield (FluorYield), on the overestimation because of the backscattered Cherenkov (CherBack) and on the uncertainty because of the geometrical reconstruction (GeoReco) are represented in the columns. Total represents the product as shown in Eq. 11.

1 angles and energy 10^{20} eV has been chosen. As can be seen, the algorithm
 2 we developed is affected by systematics which are generally within a 10%. A
 3 notable exception is represented by the Cherenkov backscattered. Contami-
 4 nation can exceed the 20%. This is expected since we are not performing
 5 any Cherenkov correction for the time being. In this way, the energy will be
 6 overestimated but the amount of additional light due to backscattering can
 7 be easily determined. The backscattered Cherenkov contamination is strongly
 8 influenced by the Rayleigh scattering anisotropy. In fact, being that the emis-
 9 sion is stronger along the photon propagation axis, the contamination will be
 10 stronger for vertical events. Another evident pattern of Tab. 1, is the worsen-
 11 ing collection capability of the algorithms at the highest zenith angles. This is
 12 due to the increasing lateral width of the shower at such angles. The spot will
 13 therefore be broader for horizontal showers. The fixed collection area we are
 14 assuming will lose efficiency when the spot increases in size. Efforts are going
 15 on to solve this discrepancy with a better spot parameterization.

16 Despite the detailed study on the systematics, we still have a residual of
 17 4–8% overestimation on all the inclinations. The final energy will be overesti-
 18 mated even after correcting the systematics of Tab. 1. The systematic study
 19 has been performed only in limited conditions. The corrections on all the
 20 samples of different energy, zenith angles and field of view positions are still
 21 underway and will require extrapolations to correct intermediate conditions
 22 as well. For this reason, we decided to represent the preliminary results as
 23 resolutions and to neglect (for the moment) the systematic shift for both the
 24 energy and the X_{\max} .

25 3 Energy resolution

26 Using the reconstruction procedure discussed in the previous Chapter, a study
 27 on the energy resolution of the JEM–EUSO mission has been performed for
 28 different zenith angles and different energies. The impact point is selected in

1 the inner ± 20 km from the center of the field of view. Showers are generated
 2 according to the GIL parameterization. We simulated 8000 events for each
 3 point and we applied quality cuts $\text{DOF} > 4$, $\chi^2/\text{Ndf} < 3$ on all the conditions.
 4 In Figs. 17 and 18, we show the energy reconstruction performances for the
 5 slant depth and Cherenkov method, respectively. To estimate the quality of
 6 the reconstruction, we defined the parameter R for each event as in Eq. 12.

$$R = \frac{E_{\text{reco}} - E_{\text{real}}}{E_{\text{real}}} \quad (12)$$

7 The distribution of the R factor for all the events which survived the cuts
 8 has then been fitted with a Gaussian curve. The σ parameter has been reported
 9 here. As said before, we ignored the average of the distributions given the non
 10 completeness of the systematics study. An example of the R distribution arising
 11 from the condition 10^{20} eV, 45 degrees has been shown in Fig. 21. We also
 12 show here the Gaussian fit on this distribution.

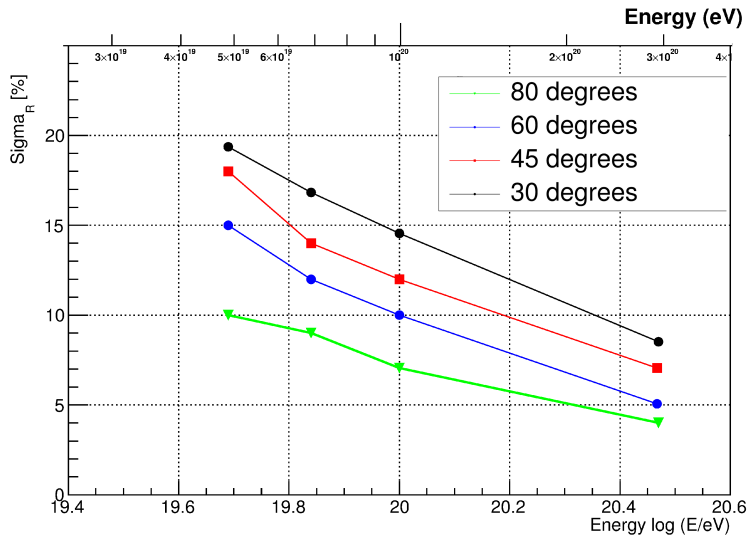


Fig. 17 the σ_R factor, namely the sigma on the distribution of all R (multiplied by 100), is shown here. Here, we plot here the results for various zenith angles and energies. All the events are impacting in the ± 20 km square. The geometry has been reconstructed with the slant depth method.

13 As can be seen in Fig. 17, the energy resolution tends to improve toward the
 14 higher zenith angles. The resolution also tends to improve with the increasing
 15 energy due to the better quality of signal for the high energy events. Generally,
 16 the slant depth method will always have a resolution under 20%. At the most
 17 extreme energies, the resolution reaches 10% or even lower.

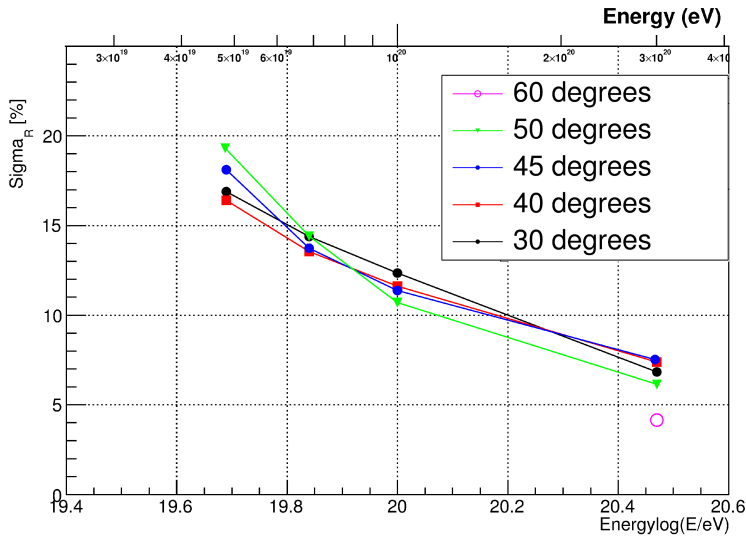


Fig. 18 the σ_R factor, namely the sigma on the distribution of all R (multiplied by 100), is shown here. Here we plot the results for various zenith angles and energies. All the events are impacting in the ± 20 km square. The geometry has been reconstructed with the Cherenkov method.

1 In Fig. 18, the energy resolution obtained with the Cherenkov method is
 2 shown. Again, the highest energies allow the best performances, while a clear
 3 improvement depending on the zenith angle cannot be seen anymore. This
 4 is due to the worsening quality of the Cherenkov peak at the highest zenith
 5 angles. In fact, the Cherenkov peak will be much more difficult to recognize at
 6 the large zenith angles due to the larger spread of this reflection spot. More-
 7 over, because of this reason, the Cherenkov method cannot be extended above
 8 50–60 degrees. The Cherenkov reconstruction can be extended at maximum
 9 at 60 degrees just for the 60 degrees events. In such cases, in fact, the strong
 10 Cherenkov signal will still allow the discrimination from background despite
 11 the high zenith angle. The lowest energies already show a loss of quality at
 12 smaller zenith angles.

13 Notably, both slant depth and Cherenkov method give comparable perfor-
 14 mances under all the conditions. Such methods can be also used as a valid
 15 cross check since they are totally independent from each other.

16 In Fig. 19, the energy resolution, estimated using the slant depth method,
 17 is shown for events distributed on the whole field of view ($\pm 270, \pm 200$) km
 18 and for energies in the range $2 \cdot 10^{19} - 2 \cdot 10^{20}$ eV. The events have zenith
 19 angles between 0 and 90 degrees distributed as $\sin(2\theta)$. Here, we also apply
 20 $\text{DOF} > 4$, $\chi^2/\text{Ndf} < 3$ quality cuts on $\sim 4 \cdot 10^4$ events. The resolution
 21 can also be observed to range from $\sim 30\%$ at $2 \cdot 10^{19}$ eV to 15–20% at \sim
 22 10^{20} eV. Systematics have not been corrected and may still be contributing to
 23 the distribution width. In general, the energy resolution is not as good as in

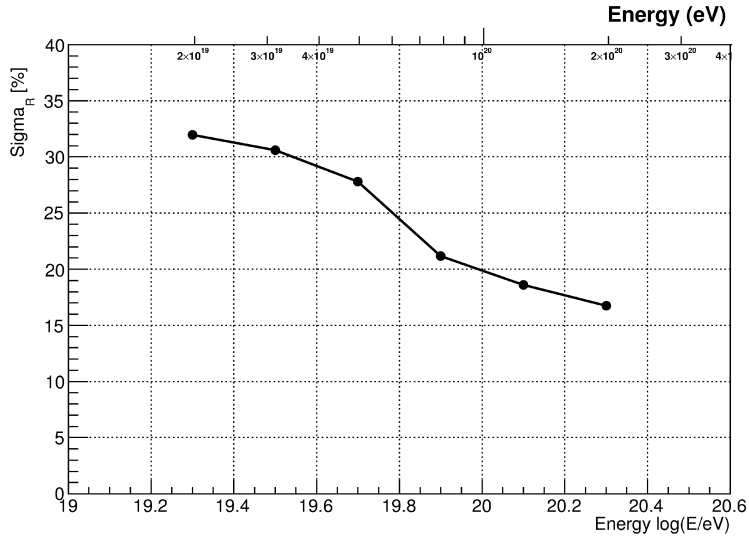


Fig. 19 The energy reconstruction performances are shown here for the all-event sample. The points represent the σ_R value (multiplied by 100). The sample with cuts $\text{DOF} > 4$, $\chi^2/\text{Ndf} < 3$ is shown here.

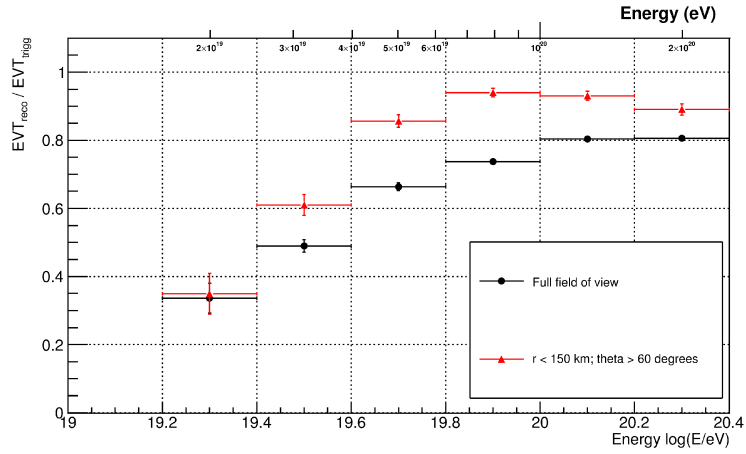


Fig. 20 the fraction of reconstructed events. We show here the fraction of events surviving the cut $\text{DOF} > 4$, $\chi^2/\text{Ndf} < 3$. The fraction is shown with respect to the triggered events. In black, we see the full-FOV curve while, in red, the curve with the cut $r < 150$ km, zenith angle > 60 degrees is shown.

- 1 the case of events impinging in the center (Fig. 17). This is expected due to
- 2 the wider set of conditions considered here with a wide range of systematics

1 involved. Moreover, the events at the edges of the field of view are characterized
 2 by worse reconstruction performances due to the worsening detector quality.

3 In Fig. 20, the fraction of events reconstructed with quality cuts DOF
 4 > 4 $\chi^2/\text{Ndf} < 3$ with respect to triggered events is shown. As can be seen,
 5 the presence of such cuts delivers a fraction of reconstructed events which is
 6 reaching 80% above $\sim 10^{20}$ eV. This fraction decreases to 35–40% at $2 \cdot 10^{19}$ eV
 7 The application of cuts on the impact point position ($r_{\text{center}} < 150$ km) and
 8 zenith angle (60 degrees) delivers a better reconstruction efficiency at the
 9 lowest energies. As can be seen in [10], the application of cuts on the field
 10 of view position and zenith angle will bring the trigger full efficiency range
 11 toward lower energies (90% at $5\text{--}6 \cdot 10^{19}$ eV). This reduces the systematics of
 12 the JEM-EUSO exposure at $4\text{--}5 \cdot 10^{19}$ eV significantly. This allows a more
 13 reliable superposition with ground arrays. The reconstruction is also behaving
 14 in a similar way as the trigger studied in [10]. The exposure will, in fact, vary
 15 just up to 10% if we consider energies of $5 \cdot 10^{19}$ eV. Further studies are
 16 needed but this result seems to show that the reconstruction is not hampering
 17 the superposition with ground arrays in a significant way.

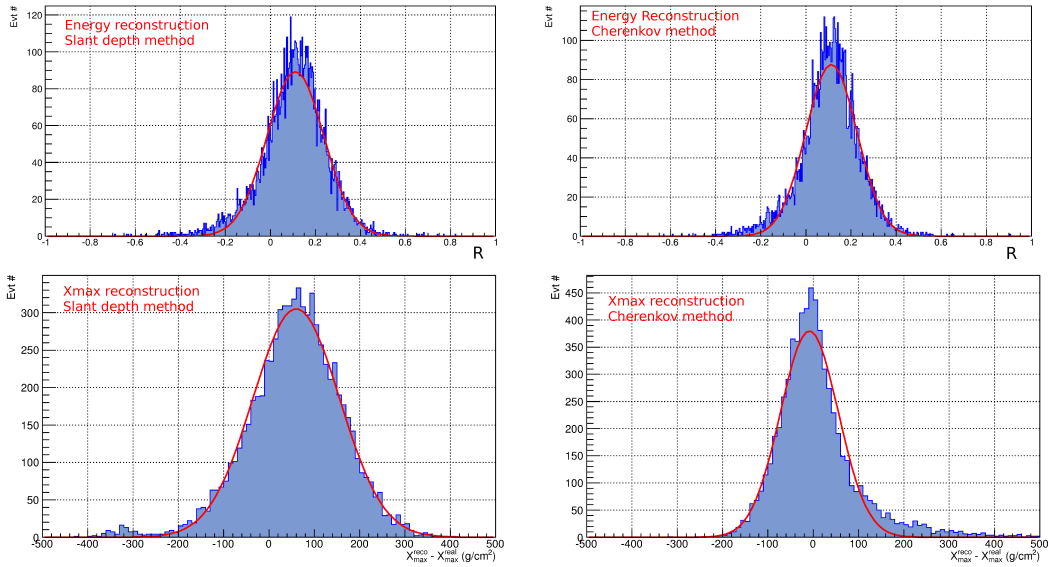


Fig. 21 we show here an example of the single point distribution shown in Fig. 17, 18 22
 23. The the resolution distributions are shown here together with the Gaussian fit. All the
 plots are calculated for the example 10^{20} eV, 45 degrees and in the $(\pm 20, \pm 20)$ km of the
 field of view.

4 X_{\max} resolution

A similar study has been performed for the X_{\max} parameter. Using the samples described in the previous section (like in Figs. 17 and 18), we have calculated the distribution of the slant depth of the maximum. In Figs. 22 and 23, we show the JEM–EUSO X_{\max} resolution for fixed conditions of zenith angle and energy. Similarly as in the case for the energy, we evaluate the parameter $X_{\max}^{\text{reco}} - X_{\max}^{\text{real}}$ for all the events. We also fit the distribution with a Gaussian and we plot the σ parameter. An example of such distributions, with the corresponding Gaussian fit, can be seen in Fig. 21.

More in detail in Fig. 22, we show the reconstruction performances for the slant depth method. As already explained in the previous sections, the result must be considered more as a test than the real performance estimation. In fact, the assumption on the X_{\max}^{geo} will cause a bias in the geometry reconstruction. The X_{\max}^{fit} plotted here will therefore be biased by the initial assumptions. The algorithm should be iterated in order to remove the dependence from any assumption. Nevertheless, this result can be seen as a proof of the establishment of the entire chain and as a test of the algorithms.

As can be seen in Fig. 22, the X_{\max} resolution improves with the energy. At the lowest energies, it ranges from 90 to 120 g/cm² while at the most extreme energies, from 60 to 80 g/cm². The higher zenith angles also bring a better resolution. This is due to the better angular resolution which can be achieved in these conditions. Moreover, the higher altitude of such events implies higher luminosities at the detector. The completeness of the profile can be also fitted and is not cut by the ground impact.

In Fig. 23, we can see the X_{\max} reconstruction performances obtained with the Cherenkov method. As can be seen here, the performances are significantly better ranging from 80–100 g/cm² at the lowest energies and 50–60 g/cm² at the highest. As already explained, at the highest zenith angles the Cherenkov reflection peak will be not recognizable. For this reason, the plots will not extend above 60 degrees.

The highest energies also display a significantly better performance. However, unlike in the slant depth case, an improvement with the zenith angle cannot be seen. In fact, the quality of the Cherenkov peaks detected at large zenith angles is expected to decrease. In the most extreme cases, at low energies, these peaks will be affected by biases that prevent the X_{\max} reconstruction. For this reason, a further selection has been performed in Fig. 23 and several points have been omitted. The X_{\max} parameters is, in fact, much more sensible to systematics in the peak position than the energy and, therefore, several points that have been accepted in the energy reconstruction cannot be accepted for X_{\max} . The 45 and 50 degrees samples have only been shown for the highest energy cases.

The Cherenkov method is, however (where applicable), much more reliable since no assumption on the X_{\max}^{geo} is done in order to reconstruct the geometry. Such results can already be considered as a preliminary estimation of the JEM–EUSO X_{\max} reconstruction capabilities.

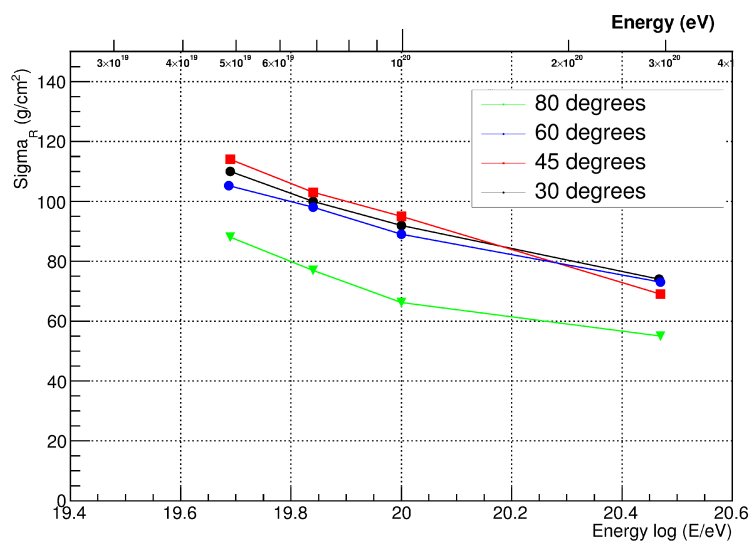


Fig. 22 the σ of the X_{\max} resolution is shown here. Here we plot the results for various zenith angles and energies. All the events are impacting in the ± 20 km square. The geometry has been reconstructed with the slant depth method.

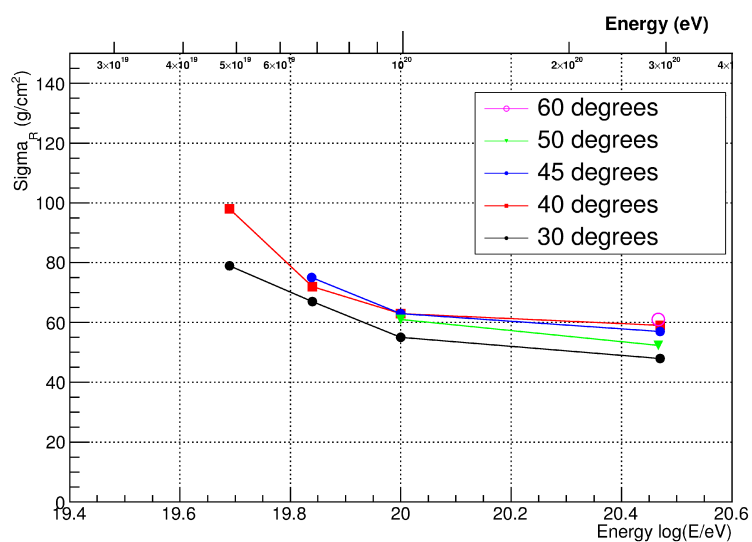


Fig. 23 the σ of the X_{\max} resolution is shown here. Here we plot the results for various zenith angles and energies. All the events are impacting in the ± 20 km square. The geometry has been reconstructed with the Cherenkov method.

5 Conclusions

Within this publication, the up-to-date JEM–EUSO energy and X_{\max} reconstruction algorithms have been described. To test the reconstruction algorithms, some preliminary example has been shown in fixed conditions, both for the energy and for X_{\max} .

In fixed conditions, the energy resolution remains within $\pm 20\%$ above $5 \cdot 10^{19}$ eV for both slant depth and Cherenkov method. The resolution always improves with the energy reaching 5–10% at $3 \cdot 10^{20}$ eV for both methods.

In fixed conditions X_{\max} is generally reconstructed within ± 120 g/cm² for the slant depth method and within ± 100 g/cm² for the Cherenkov method. Here both algorithms also improve with the increasing energy reaching ~ 50 g/cm² in both cases at $3 \cdot 10^{20}$ eV. The Cherenkov method will generally deliver a significantly better X_{\max} resolution, especially for low zenith angles. The slant depth method gives an X_{\max} resolution which improves with the zenith angle, while the Cherenkov method shows a roughly zenith angle-independent performance.

The detection of a Cherenkov mark will allow a better energy and X_{\max} reconstruction and will offer the possibility of a cross calibration of the two methods. A subclass of events will be reconstructed with the Cherenkov method which presents the best performances. In all of the cases where no Cherenkov peak will be detected, the slant depth method will be used.

The energy reconstruction performances have also been studied on the entire FOV and for zenith angles from 0 to 90 degrees but only with the slant depth method. On the all-event sample (Fig. 19), the resolution is $\pm 15\%$ at $2 \cdot 10^{20}$ eV, while at the lowest energies it is $\pm 30\%$. We compare these results with the ones obtained in the center, which are always below 20%. The application of field of view cuts will, therefore, certainly improve the resolution.

In Fig. 20, an example of the reconstructed fraction after the application of basic cuts is shown as function of the energy on the all-events sample. As can be seen, around $5 \cdot 10^{19}$ eV between 65% and 80% of the triggered events can be reconstructed depending on the position and zenith angle selection cuts. The application cuts on the impact position and on the zenith angle will deliver a higher efficiency at the lowest energies. This shows how a superposition with ground arrays is possible, however, more detailed studies are needed.

6 Acknowledgments

We wish to thank the RIKEN Integrated Cluster of Clusters facility for the computer resources used for the calculations. We also wish to thank the original ESAF developers for their work.

References

1. Takahashi Y. et al, 2009 The JEM–EUSO Mission *New. J. of Phys.* **11** 065009.

- 1 2. J. Adams et al for the JEM–EUSO collaboration, "Ultra High Energy Cosmic Rays
2 studies with the JEM–EUSO mission", *Experimental Astronomy Journal*, this Issue's
3 number 2 contribution.
- 4 3. G.A. Medina Tanco for the JEM–EUSO collaboration, "The JEM–EUSO Science capa-
5 bilities", proceeding of the Int. Cosmic Ray Conference (Rio De Janeiro) (2013) – ID
6 0956
- 7 4. The JEM–EUSO collaboration, "Report on the phase A study 2010", Collaboration
8 Mission Report (2010)
- 9 5. F. Kajino for the JEM–EUSO collaboration, "The JEM–EUSO instruments", proceeding
10 of the Int. Cosmic Ray Conference (Rio De Janeiro) (2013) – ID1216
- 11 6. M. Casolino, F. Kajino, "An overview of the JEM–EUSO instrument", this Issue's num-
12 ber 8 contribution.
- 13 7. S. Dagoret, P. Barrillon, A. Jung, A. Ebersoldt, "The Photodetector Module of the JEM–
14 EUSO mission", this Issue's number 9 contribution.
- 15 8. C. Berat et al., "ESAF: Full Simulation of Space–Based Extensive Air Showers Detec-
16 tors", *Astrop. Phys. Vol. 33, 4*, P. 221–247 (2010)
- 17 9. M. Bertaina et al., "Performance and air-shower reconstruction techniques for the JEM–
18 EUSO mission", *Advances in Space Res.*, Volume 53, Issue 10, 15 May 2014, Pages
19 1515–1535
- 20 10. The JEM–EUSO collaboration, "An evaluation of the exposure in nadir observation of
21 the JEM–EUSO mission", *Astroparticle Physics* 44 (2013) 76–90
- 22 11. A. Guzman et al., "The Peak and Window Searching Technique for the EUSO Simula-
23 tion and Analysis Framework: Impact on the Angular Reconstruction of EAS.", *Jour. of*
24 *Phys.: Conf. Series* 409 (2013) 012104
- 25 12. T. Mernik, A. Guzman, S. Biktemerova, "Performances of JEM–EUSO: angular recon-
26 struction", this Issue's number 10 contribution.
- 27 13. D. Gora et al., "Universal lateral distribution of energy deposit in air showers and its
28 application to shower reconstruction", *Astrop. Phys. Vol. 24.*, P. 484–494 (2006)
- 29 14. National Oceanic Atmospheric Administration et al., "U.S standard atmosphere, 1976",
30 public document (1976)
- 31 15. M. Giller et al., "Energy spectra of electrons in the extensive air showers of ultra-high
32 energy", *J. Phys. G: Nucl. Part. Phys. V 30*, P97–105 (2004)
- 33 16. Air Force Geophysics Laboratory, "Users guide to LOWTRAN 7", public document
34 (1988)
- 35 17. M. Nagano, "New measurement on photon yields from air and the application to the
36 energy estimation of primary cosmic rays", arXiv:astro-ph/0406474v2 (2004)
- 37 18. M. Unger et al., "Reconstruction of longitudinal profiles of ultra-high energy cosmic ray
38 showers from fluorescence and Cherenkov light measurements", *Nucl. Instr. and Met. in*
39 *Phys. Res. A* 588 (2008)
- 40 19. D. Naumov, "SLAST, Shower Light Attenuated to the Space Telescope", EUSO mission
41 internal document (2003)
- 42 20. B. Rossi, "Cosmic-Ray Theory", K. Greisen, *Rev. Mod. Phys*, 13 , 240 (1941)
- 43 21. N. P. Ilina et al., *Sov. J. Nucl. Phys.* 55, 1540 (1992)
- 44 22. N. N. Kalmykov, S. S. Ostapchenko, *Sov. J. Nucl. Phys.* 50, 315 (1989)
- 45 23. F. Fenu, "A simulation study of the JEM–EUSO mission for the detection of ultra-high
46 energy Cosmic Rays", Doctoral Thesis, (2013)

The JEM-EUSO Collaboration

3 J.H. Adams Jr.^{md}, S. Ahmad^{bb}, J.-N. Albert^{ba}, D. Allard^{bc}, L. Anchordoqui^{mf}, V. Andreev^{me},
 4 A. Anzalone^{dh,dn}, Y. Arai^{ev}, K. Asano^{et}, M. Ave Pernas^{kc}, P. Baragatti^{do}, P. Barrillon^{ba},
 5 T. Batsch^{hc}, J. Bayer^{cd}, R. Bechini^{dl}, T. Belenguer^{kb}, R. Bellotti^{da,db}, K. Belov^{me}, A.A. Berlind^{mh},
 6 M. Bertaina^{dk,dl}, P.L. Biermann^{cb}, S. Biktemerova^{ia}, C. Blaksley^{bc}, N. Blanc^{ta}, J. Błęcki^{hd},
 7 S. Blin-Bondil^{bb}, J. Blümer^{cb}, P. Bobik^{ja}, M. Bogomilov^{aa}, M. Bonamente^{md}, M.S. Briggs^{md},
 8 S. Briz^{kd}, A. Bruno^{da}, F. Cafagna^{da}, D. Campana^{df}, J.-N. Capdevielle^{bc}, R. Caruso^{dc,dn},
 9 M. Casolino^{ew,di}, C. Cassardo^{dk,dl}, G. Castellini^{dd}, C. Catalano^{bd}, O. Catalano^{dh,dn}, A. Cellino^{dk,dm},
 10 M. Chikawa^{ed}, M.J. Christl^{mg}, D. Cline^{me}, V. Connaughton^{md}, L. Conti^{do}, G. Cordero^{ga},
 11 H.J. Crawford^{ma}, R. Cremonini^{dl}, S. Csorna^{mh}, S. Dagoret-Campagne^{ba}, A.J. de Castro^{kd},
 12 C. De Donato^{di}, C. de la Taille^{bb}, C. De Santis^{di,dj}, L. del Peral^{kc}, A. Dell’Oro^{dk,dm}, N. De
 13 Simone^{di}, M. Di Martino^{dk,dm}, G. Distratis^{cd}, F. Dulucq^{bb}, M. Dupieux^{bd}, A. Ebersoldt^{cb},
 14 T. Ebisuzaki^{ew}, R. Engel^{cb}, S. Falk^{cb}, K. Fang^{mb}, F. Fenu^{cd}, I. Fernández-Gómez^{kd}, S. Ferrarese^{dk,dl},
 15 D. Finco^{do}, M. Flaminio^{do}, C. Fornaro^{do}, A. Franceschi^{de}, J. Fujimoto^{ev}, M. Fukushima^{eg},
 16 P. Galeotti^{dk,dl}, G. Garipovic^{ic}, J. Geary^{md}, G. Gelmini^{me}, G. Giraud^{dk}, M. Gonchar^{ia},
 17 C. González Alvarado^{kb}, P. Gorodetzky^{bc}, F. Guarino^{df,dg}, A. Guzmán^{cd}, Y. Hachisu^{ew},
 18 B. Harlov^{ib}, A. Haungs^{cb}, J. Hernández Carretero^{kc}, K. Higashide^{er,ew}, D. Ikeda^{eg}, H. Ikeda^{ep},
 19 N. Inoue^{er}, S. Inoue^{eg}, A. Insolia^{dc,dn}, F. Isgrò^{df,dp}, Y. Itow^{en}, E. Joven^{ke}, E.G. Judd^{ma},
 20 A. Jung^{fb}, F. Kajino^{ei}, T. Kajino^{el}, I. Kaneko^{ew}, Y. Karadzhov^{aa}, J. Karczmarczyk^{hc},
 21 M. Karus^{cb}, K. Katahira^{ew}, K. Kawai^{ew}, Y. Kawasaki^{ew}, B. Keilhauer^{cb}, B.A. Khrenov^{ic},
 22 Jeong-Sook Kim^{fa}, Soon-Wook Kim^{fa}, Sug-Whan Kim^{fd}, M. Kleifges^{cb}, P.A. Klimov^{ic},
 23 D. Kolev^{aa}, I. Kreykenbohm^{ca}, K. Kudela^{ja}, Y. Kurihara^{ev}, A. Kusenko^{me}, E. Kuznetsov^{md},
 24 M. Lacombe^{bd}, C. Lachaud^{bc}, J. Lee^{fc}, J. Licandro^{ke}, H. Lim^{fc}, F. López^{kd}, M.C. Maccarone^{dh,dn},
 25 K. Mannheim^{ce}, D. Maravilla^{ga}, L. Marcelli^{dj}, A. Marini^{de}, O. Martinez^{gc}, G. Masciantonio^{di,dj},
 26 K. Mase^{ea}, R. Matev^{aa}, G. Medina-Tanco^{ga}, T. Mernik^{cd}, H. Miyamoto^{ba}, Y. Miyazaki^{ec},
 27 Y. Mizumoto^{el}, G. Modestino^{de}, A. Monaco^{da,db}, D. Monnier-Ragaigne^{ba}, J.A. Morales de
 28 los Ríos^{ka,kc}, C. Moretto^{ba}, V.S. Morozenko^{ic}, B. Mot^{bd}, T. Murakami^{ef}, M. Nagano^{ec},
 29 M. Nagata^{eh}, S. Nagataki^{ek}, T. Nakamura^{ej}, T. Napolitano^{de}, D. Naumov^{ia}, R. Nava^{ga},
 30 A. Neronov^{lb}, K. Nomoto^{eu}, T. Nonaka^{eg}, T. Ogawa^{ew}, S. Ogio^{eo}, H. Ohmori^{ew}, A.V. Olinto^{mb},
 31 P. Orleński^{hd}, G. Osteria^{df}, M.I. Panasyuk^{ic}, E. Parizot^{bc}, I.H. Park^{fc}, H.W. Park^{fc},
 32 B. Pastircak^{ja}, T. Patzak^{bc}, T. Paul^{mf}, C. Pennypacker^{ma}, S. Perez Cano^{kc}, T. Peter^{lc},
 33 P. Picozza^{di,dj,ew}, T. Pierog^{cb}, L.W. Piotrowski^{ew}, S. Piraino^{cd,dh}, Z. Plebaniak^{hc}, A. Pollini^{la},
 34 P. Prat^{bc}, G. Prévôt^{bc}, H. Prieto^{kc}, M. Putis^{ja}, P. Reardon^{md}, M. Reyes^{ke}, M. Ricci^{de},
 35 I. Rodríguez^{kd}, M.D. Rodríguez Frías^{kc}, F. Ronga^{de}, M. Roth^{cb}, H. Rothkaehl^{hd}, G. Roudil^{bd},
 36 I. Rusinov^{aa}, M. Rybczyński^{ha}, M.D. Sabau^{kb}, G. Sáez Cano^{kc}, H. Sagawa^{eg}, A. Saito^{ej},
 37 N. Sakaki^{cb}, M. Sakata^{ei}, H. Salazar^{gc}, S. Sánchez^{kd}, A. Santangelo^{cd}, L. Santiago Cruz^{ga},
 38 M. Sanz Palomino^{kb}, O. Saprykin^{ib}, F. Sarazin^{mc}, H. Sato^{ei}, M. Sato^{es}, T. Schanz^{cd},
 39 H. Schieler^{cb}, V. Scotti^{df,dg}, A. Segreto^{dh,dn}, S. Selman^{bc}, D. Semikoz^{bc}, M. Serra^{ke},
 40 S. Sharakin^{ic}, T. Shibata^{eq}, H.M. Shimizu^{em}, K. Shinozaki^{ew,cd}, T. Shirahama^{er}, G. Siemieniec-
 41 Oziębło^{hb}, H.H. Silva López^{ga}, J. Sledd^{mg}, K. Słomińska^{hd}, A. Sobey^{mg}, T. Sugiyama^{em},
 42 D. Supanitsky^{ga}, M. Suzuki^{ep}, B. Szabelska^{hc}, J. Szabelski^{hc}, F. Tajima^{ee}, N. Tajima^{ew},
 43 T. Tajima^{cc}, Y. Takahashi^{es}, H. Takami^{ev}, M. Takeda^{eg}, Y. Takizawa^{ew}, C. Tenzer^{cd},
 44 O. Tibolla^{ce}, L. Tkachev^{ia}, H. Tokuno^{et}, T. Tomida^{ew}, N. Tone^{ew}, S. Toscano^{lb}, F. Trillaud^{ga},
 45 R. Tsenov^{aa}, Y. Tsunesada^{et}, K. Tsuno^{ew}, T. Tymieniecka^{hc}, Y. Uchihori^{eb}, M. Unger^{cb},
 46 O. Vaduvescu^{ke}, J.F. Valdés-Galicia^{ga}, P. Vallania^{dk,dm}, L. Valore^{df,dg}, G. Vankova^{aa},
 47 C. Vigorito^{dk,dl}, L. Villaseñor^{gb}, P. von Ballmoos^{bd}, S. Wada^{ew}, J. Watanabe^{el}, S. Watanabe^{es},
 48 J. Watts Jr.^{md}, M. Weber^{cb}, T.J. Weiler^{mh}, T. Wibig^{hc}, L. Wiencke^{mc}, M. Wille^{ca}, J. Wilms^{ca},
 49 Z. Włodarczyk^{ha}, T. Yamamoto^{ei}, Y. Yamamoto^{ei}, J. Yang^{fb}, H. Yano^{ep}, I.V. Yashin^{ic},
 50 D. Yonetoku^{ef}, K. Yoshida^{ei}, S. Yoshida^{ea}, R. Young^{mg}, M. Yu. Zotov^{ic}, A. Zuccaro Marchi^{ew}

51 ^{aa} St. Kliment Ohridski University of Sofia, Bulgaria

52 ^{ba} LAL, Univ Paris-Sud, CNRS/IN2P3, Orsay, France

53 ^{bb} Omega, Ecole Polytechnique, CNRS/IN2P3, Palaiseau, France

54 ^{bc} APC, Univ Paris Diderot, CNRS/IN2P3, CEA/Irfu, Obs. de Paris, Sorbonne Paris Cité, France

- 1 *bd* IRAP, Université de Toulouse, CNRS, Toulouse, France
 2 *ca* ECAP, University of Erlangen-Nuremberg, Germany
 3 *cb* Karlsruhe Institute of Technology (KIT), Germany
 4 *cc* Ludwig Maximilian University, Munich, Germany
 5 *cd* Inst. for Astronomy and Astrophysics, Kepler Center, University of Tübingen, Germany
 6 *ce* Institut für Theoretische Physik und Astrophysik, University of Würzburg, Germany
 7 *da* Istituto Nazionale di Fisica Nucleare - Sezione di Bari, Italy
 8 *db* Università degli Studi di Bari Aldo Moro and INFN - Sezione di Bari, Italy
 9 *dc* Dipartimento di Fisica e Astronomia - Università di Catania, Italy
 10 *dd* Consiglio Nazionale delle Ricerche (CNR) - Ist. di Fisica Applicata Nello Carrara, Firenze, Italy
 11 *de* Istituto Nazionale di Fisica Nucleare - Laboratori Nazionali di Frascati, Italy
 12 *df* Istituto Nazionale di Fisica Nucleare - Sezione di Napoli, Italy
 13 *dg* Università di Napoli Federico II - Dipartimento di Scienze Fisiche, Italy
 14 *dh* INAF - Istituto di Astrofisica Spaziale e Fisica Cosmica di Palermo, Italy
 15 *di* Istituto Nazionale di Fisica Nucleare - Sezione di Roma Tor Vergata, Italy
 16 *dj* Università di Roma Tor Vergata - Dipartimento di Fisica, Roma, Italy
 17 *dk* Istituto Nazionale di Fisica Nucleare - Sezione di Torino, Italy
 18 *dl* Dipartimento di Fisica, Università di Torino, Italy
 19 *dm* Osservatorio Astrofisico di Torino, Istituto Nazionale di Astrofisica, Italy
 20 *dn* Istituto Nazionale di Fisica Nucleare - Sezione di Catania, Italy
 21 *do* UTIU, Dipartimento di Ingegneria, Rome, Italy
 22 *dp* DIETI, Università degli Studi di Napoli Federico II, Napoli, Italy
 23 *ea* Chiba University, Chiba, Japan
 24 *eb* National Institute of Radiological Sciences, Chiba, Japan
 25 *ec* Fukui University of Technology, Fukui, Japan
 26 *ed* Kinki University, Higashi-Osaka, Japan
 27 *ee* Hiroshima University, Hiroshima, Japan
 28 *ef* Kanazawa University, Kanazawa, Japan
 29 *eg* Institute for Cosmic Ray Research, University of Tokyo, Kashiwa, Japan
 30 *eh* Kobe University, Kobe, Japan
 31 *ei* Konan University, Kobe, Japan
 32 *ej* Kyoto University, Kyoto, Japan
 33 *ek* Yukawa Institute, Kyoto University, Kyoto, Japan
 34 *el* National Astronomical Observatory, Mitaka, Japan
 35 *em* Nagoya University, Nagoya, Japan
 36 *en* Solar-Terrestrial Environment Laboratory, Nagoya University, Nagoya, Japan
 37 *eo* Graduate School of Science, Osaka City University, Japan
 38 *ep* Institute of Space and Astronautical Science/JAXA, Sagamihara, Japan
 39 *eq* Aoyama Gakuin University, Sagamihara, Japan
 40 *er* Saitama University, Saitama, Japan
 41 *es* Hokkaido University, Sapporo, Japan
 42 *et* Interactive Research Center of Science, Tokyo Institute of Technology, Tokyo, Japan
 43 *eu* University of Tokyo, Tokyo, Japan
 44 *ev* High Energy Accelerator Research Organization (KEK), Tsukuba, Japan
 45 *ew* RIKEN, Wako, Japan
 46 *fa* Korea Astronomy and Space Science Institute (KASI), Daejeon, Republic of Korea
 47 *fb* Ewha Womans University, Seoul, Republic of Korea
 48 *fc* Sungkyunkwan University, Seoul, Republic of Korea
 49 *fd* Center for Galaxy Evolution Research, Yonsei University, Seoul, Republic of Korea
 50 *ga* Universidad Nacional Autónoma de México (UNAM), Mexico
 51 *gb* Universidad Michoacana de San Nicolas de Hidalgo (UMSNH), Morelia, Mexico
 52 *gc* Benemérita Universidad Autónoma de Puebla (BUAP), Mexico
 53 *ha* Jan Kochanowski University, Institute of Physics, Kielce, Poland
 54 *hb* Jagiellonian University, Astronomical Observatory, Krakow, Poland
 55 *hc* National Centre for Nuclear Research, Lodz, Poland
 56 *hd* Space Research Centre of the Polish Academy of Sciences (CBK), Warsaw, Poland
 57 *ia* Joint Institute for Nuclear Research, Dubna, Russia
 58 *ib* Central Research Institute of Machine Building, TsNIIMash, Korolev, Russia

-
- 1 ^{*ic*} Skobeltsyn Institute of Nuclear Physics, Lomonosov Moscow State University, Russia
 - 2 ^{*ja*} Institute of Experimental Physics, Kosice, Slovakia
 - 3 ^{*ka*} Consejo Superior de Investigaciones Científicas (CSIC), Madrid, Spain
 - 4 ^{*kb*} Instituto Nacional de Técnica Aeroespacial (INTA), Madrid, Spain
 - 5 ^{*kc*} Universidad de Alcalá (UAH), Madrid, Spain
 - 6 ^{*kd*} Universidad Carlos III de Madrid, Spain
 - 7 ^{*ke*} Instituto de Astrofísica de Canarias (IAC), Tenerife, Spain
 - 8 ^{*la*} Swiss Center for Electronics and Microtechnology (CSEM), Neuchâtel, Switzerland
 - 9 ^{*lb*} ISDC Data Centre for Astrophysics, Versoix, Switzerland
 - 10 ^{*lc*} Institute for Atmospheric and Climate Science, ETH Zürich, Switzerland
 - 11 ^{*ma*} Space Science Laboratory, University of California, Berkeley, USA
 - 12 ^{*mb*} University of Chicago, USA
 - 13 ^{*mc*} Colorado School of Mines, Golden, USA
 - 14 ^{*md*} University of Alabama in Huntsville, Huntsville, USA
 - 15 ^{*me*} University of California (UCLA), Los Angeles, USA
 - 16 ^{*mf*} University of Wisconsin-Milwaukee, Milwaukee, USA
 - 17 ^{*mg*} NASA - Marshall Space Flight Center, USA
 - 18 ^{*mh*} Vanderbilt University, Nashville, USA
 - 19